Resonant frequency and bandwidth of metamaterial emitters and absorbers predicted by an RLC circuit model

CrossMark

Atsushi Sakurai [a,b], Bo Zhao [a], Zhuomin M. Zhang [a,*]

[a] George W. Woodruff School of Mechanical Engineering, Georgia Institute of Technology, Atlanta, GA 30332, USA
[b] Department of Mechanical and Production Engineering, Niigata University, 8050, Ikarashi 2-no-cho, Niigata 950-2181, Japan

ARTICLE INFO

ABSTRACT

Metamaterial thermal emitters and absorbers have been widely studied for different geometric patterns by exciting a variety of electromagnetic resonances. A resistor–inductor–capacitor (RLC) circuit model is developed to describe the magnetic resonances (i.e. magnetic polaritons) inside the structures. The RLC circuit model allows the prediction of not only the resonance frequency, but also the full width at half maximum and quality factor for various geometric patterns. The parameters predicted by the RLC model are compared with the finite-difference time-domain simulation. The magnetic field distribution and the power dissipation density profile are also used to justify the RLC circuit model. The geometric effects on the resonance characteristics are elucidated in the wire (or strip), cross, and square patterned metamaterial in the infrared region. This study will facilitate the design of metamaterial absorbers and emitters based on magnetic polaritons.

1. Introduction

Micro/nanostructured materials have drawn great attention due to their potential applications [1–3], such as thermophotovoltaic emitters [4,5], selective solar absorbers [6,7], and biological sensors [8]. Most electromagnetic metamaterials consist of periodic nano/microstructures that exhibit exotic characteristics by excitation of resonances [9]. These phenomena are usually impossible to realize with naturally existing materials [10]. Metamaterials have a great potential as perfect emitters or absorbers of thermal radiation at certain spectral bands. Landy et al. [11] experimentally demonstrated selective absorption in the infrared region with a metallic pattern and a bottom metallic film separated by a dielectric spacer. More recently, various types of metamaterial structures with

different top patterns have been proposed and fabricated as wavelength-selective emitters and absorbers. Strong confinement of the electromagnetic energy could be achieved between the metallic pattern and the film due to electric and magnetic resonances. Liu et al. [12] demonstrated nearly perfect absorption at the wavelength of 6 μm by a cross-patterned metamaterial. Aydin et al. [13] developed an ultrathin plasmonic absorber with a nanostructured top silver film composed of crossed trapezoidal arrays in the visible spectrum.

Absorption and emission characteristics of metamaterials, such as the resonant frequency, strongly depend on the geometric shape and size of the top metallic patterns. Wang and Zhang [14] numerically showed that high-performance selective thermophotovoltaic emitter could be achieved with a metal film-coupled 1D tungsten grating structure. They also experimentally studied the selective mid-infrared absorption behavior of a film-coupled 1D gold grating structure [15]. Zhao et al. [16] proposed a selective thermophotovoltaic emitter made of a film-coupled 2D tungsten

square pattern, which exhibits strong wavelength selectivity as well as angular and polarization independence. Wang and Wang [17] investigated a broadband perfect selective metamaterial solar absorber made of 2D double-sized metamaterial absorbers. Bouchon et al. [18] and Hendrickson et al. [19] experimentally demonstrated broadband absorption of metamaterial absorbers with differently sized square patterns.

A simple analytical method to predict the resonance conditions is desired for the design of single-, dual-, and multi-band metamaterial absorbers and emitters made of film-coupled metallic patterns. Different theories have been proposed, such as the transmission line theory [20], interference theory [21], and coupled mode theory [22]. The predictions of these theories show good agreement with simulation and/or experiments for specific structures. However, an easy to apply and general approach is still lacking. Since antiparallel currents can occur in the top metallic structure and bottom metallic film under an incident time-varying magnetic field [16], magnetic polaritons (MPs) can be a plausible explanation for the resonances in those structures. An LC (inductor–capacitor) circuit model [23,24] has been successfully applied to predict the resonance frequency. In addition to the resonance frequency, the bandwidth of the absorption (or emission) peak is also important for the design of metamaterial absorbers (or emitters).

In the present work, an RLC (resistor–inductor–capacitor) circuit model is developed in order to predict the resonance characteristics, such as the frequency, full width at half maximum (FWHM), and quality factor (Q). Although RLC circuit models have been applied to metamaterials consisting of pairs of parallel slabs and fishnet structures [25–27], the present study focuses on the resonance conditions for metamaterial absorbers and emitters with different shapes of top metallic pattern over a bottom metallic film. The applicability of the RLC circuit model is explored for various geometric patterns by comparison with the finite-difference time-domain (FDTD) simulation. Geometric effects on the resonance characteristics for metamaterials with the wire (or strip), cross, and square patterns are investigated in the infrared region. The physical mechanisms for the enhanced selective absorption and emission are discussed, and the behaviors of MPs are elucidated with the magnetic field distribution, power dissipation profile, and the RLC circuit model.

2. Geometric effects on the resonance frequency and bandwidth

Two types of patterns are considered to elucidate the mechanisms for the enhanced absorption and emission and the geometric effect. The structure contains a 2D periodic metal pattern over a dielectric film which is placed atop of a metal film. The bottom metal film is opaque to infrared radiation and can easily be fabricated on a suitable substrate. The structure without the substrate is illustrated in Fig. 1, with different top metallic structures made of wire (or strip), cross, or square patterns. The parameters of the metamaterial structures used in the simulations are listed in Table 1. The period of the unit cell is $\Lambda = 3.2$ μm in both the x and y directions for each case, and the thickness of the dielectric spacer is fixed

to $d = 140$ nm. The patterned Au structures are located at the center of the unit cell and Al_2O_3 film is used as the dielectric spacer. The geometries of the patterned structures are described by the characteristic length, which is the width $w = 1.7$ μm, and thickness $h = 100$ nm. The wire pattern can be gradually transformed to the square pattern with increasing y-directional length l. Thus, a parameter sweep of l from 0.3 μm to 1.7 μm will be conducted to show the geometric effects on the MPs in the wire patterned structure. When the side length l of the two wires in the cross pattern are simultaneously varied from 0.3 μm to 1.7 μm, the cross pattern can also be transformed to the square pattern. Some geometric effects on the resonance frequency of these patterns have been investigated in the previous studies [11–19,24]. Although the aforementioned designs exhibit excellent absorption and emission efficiencies, previous studies have explored for specific structures only without considering the effect of the y-dimensional length on the resonance frequency and bandwidth. Therefore, how to explain the effect of l on the resonant frequency and bandwidth quantitatively is the interest of the present study.

The full-wave simulation based on Lumerical FDTD software is used to demonstrate the geometric effects. Periodic boundary conditions are used along the x and y directions. Perfectly-matched-layers boundary conditions are applied along the propagation direction of electromagnetic waves (the z direction). A broadband linearly polarized plane wave is incident to the unit cell from above the structure. A frequency-domain power monitor is placed above the plane wave source to collect the reflected waves. Only the transverse magnetic (TM) wave is simulated for which MPs can be excited by the y component of the magnetic field. Since the considered patterns are symmetric, the reflectance would be the same for both transverse electric (TE) and TM waves. The spectral-directional emittance is equal to the spectral-directional absorptance according to Kirchhoff's law [10], which is one minus the reflectance providing that the bottom metallic film is opaque. The normal specular reflectance is simulated from the FDTD, and the surface roughness effect is neglected in the simulation. The dependence of emittance on incident angles is expected to be insignificant because the y component of the magnetic field, which excites the magnetic resonance, does not change when the incidence angle changes [14,16]. All the simulations in this paper are performed in three-dimensional computational domain using non-uniform structured mesh with a minimum mesh size of 1 nm. Alumina (Al_2O_3) is chosen for a dielectric spacer and gold is chosen as metallic topping. The dielectric functions of alumina and gold are obtained with the tabulated data from Palik [28]. Here, the refractive index of alumina is assumed to be constant as $n = 1.57$.

Fig. 2 indicates how the normal emittance changes with the length l in the spectral region from 30 THz to 60 THz (corresponding to wavelength λ from 10 μm to 5 μm). When the length l changes from 0.3 μm to 1.7 μm, the normal emittance is significantly enhanced, and the resonant peak shifts to lower frequency with larger length l for both cases. The resonance frequencies of the cross pattern are slightly higher than that of the wire pattern
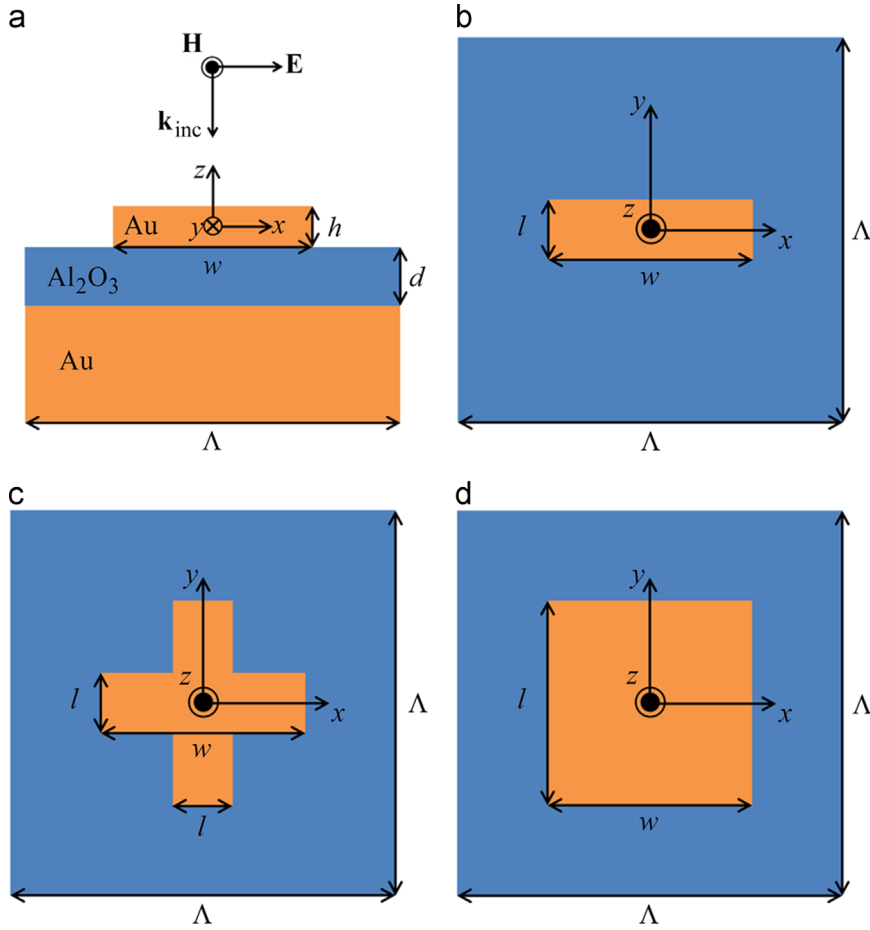
Fig. 1. Schematic of the metamaterial structure as a wavelength-selective infrared emitter or absorber. (a) The x–z plane at y=0 nm, and top view of the x–y plane of the (b) wire, (c) cross, and (d) square pattern. Unit cells are shown that include the top metal (Au) pattern over a bottom metal film, separated by a dielectric spacer (Al$_2$O$_3$).

Table 1

Geometric parameters for the metamaterial structure used in the present study.

Period	Λ [μm]	3.2
Thickness of top metallic pattern	h [nm]	100
Thickness of dielectric spacer	d [nm]	140
Characteristic length (width)	w [μm]	1.7
y-Directional length (wire)	l [μm]	0.3–1.7
y-Directional length (cross)	l [μm]	0.3–1.7

when the length l is from 0.3 μm to 1.5 μm. At $l=1.7$ μm, the spectra overlap because both the wire and cross patterns transform to the square pattern. Also, the bandwidths of the resonance peaks become broader with increasing lengths l for both patterns. These resonance peaks are originated from MPs, which are demonstrated next with a visualization of the electromagnetic field distribution. For this structure, surface plasmon polariton (SPP) occurs at $\lambda=3.2$ μm (93.7 THz) at normal incidence. Moreover, higher-order MP modes and coupled modes can occur at frequencies higher than 100 THz. Additional MPs can be excited by the strip with a length l in the x-direction for the cross pattern and the resonance frequency is also

higher than 100 THz. The focus of the present study is the zero-order MP modes in the mid-infrared region as shown in Fig. 2.

Fig. 3 shows the electromagnetic field profile along the x–z plane at y=0 nm at the resonant frequency (f_r) with different geometries: (a) wire ($l=0.5$ μm, $f_r=47.5$ THz), (b) cross ($l=0.5$ μm, $f_r=50.8$ THz), and (c) square ($l=1.7$ μm, $f_r=44.3$ THz) pattern, respectively. The contours show the strength of magnetic field normalized to that of the incidence, indicating the highly localized H field enhancement inside the Al$_2$O$_3$ spacer. The arrows show the electric field vectors, indicating the direction and strength of induced conduction current. A detailed analysis shows that the full current in the structure when MPs are excited will always form a closed loop [16], which creates a strongly enhanced magnetic field and thus forms an MP. Fig. 4 shows the magnetic field profile when the MP is excited of the x–y cross section at the center of dielectric layer which is at $z=-120$ nm with the same conditions as Fig. 3. Clearly, there is a strong confinement of electromagnetic energy inside the Al$_2$O$_3$ spacer between the top metallic pattern and bottom film. Since the area of the line pattern is relatively small, the enhancement is stronger in
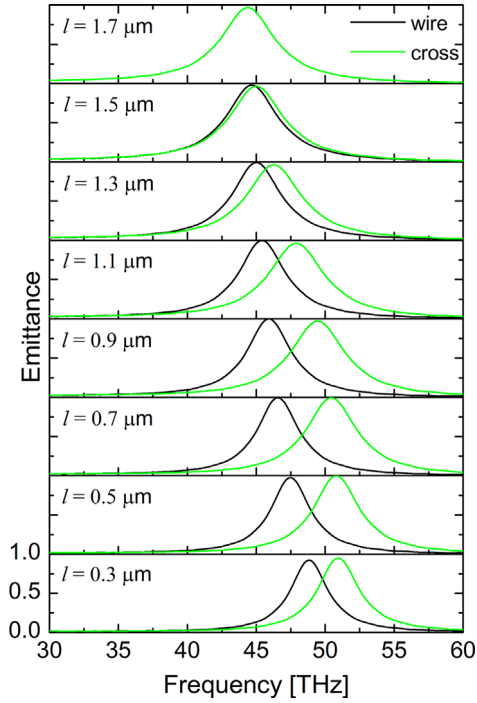
Fig. 2. Normal emittance of the metamaterial made of wire, cross, and square patterns with different length l. The y-axis range is from 0 to 1 in all panels.

the wire pattern metamaterial compared with the other two. These field patterns characterize the existence of MPs.

In previous studies, an analytical LC circuit model is employed to explain the MPs in 1D gratings and 2D patches structures [16–19,29,30]. Based on the electromagnetic field and charge distribution of the structures when the MPs are excited, the prediction of resonance conditions by the LC circuit model agreed reasonably well with numerical simulations. In addition to the resonance wavelength, FWHMs and Q-factors are also important design parameters to develop metamaterial emitters and absorbers. The FWHM is defined as the bandwidth of frequencies on either side of a resonance curve at which the emission reaches half its maximum intensity. The Q-factor equals to the resonant frequency over the bandwidth, and a higher Q-factor indicates stronger resonant response with low energy loss. An RLC circuit model is introduced to scrutinize the resonance characteristics as discussed in the next section.

3. Development of the RLC circuit model

The LC circuit model has been successfully used to understand the physical mechanisms and the geometric effects on MP [24]. However, the model is limited for the prediction of resonant frequency. In order to extend LC circuit models and to explore the resonance characteristics, we introduce an RLC circuit model because the field and current configurations for the MP can be accounted for by an equivalent RLC circuit model as shown in Fig. 5. The difference from the parallel wire model used previously [26] is that, in the present study, the resistance and kinetic
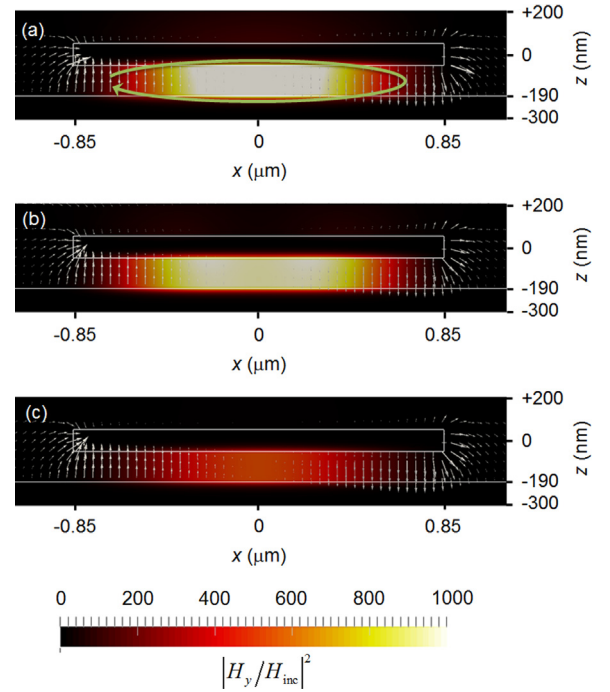
Fig. 3. Electromagnetic field profiles at the resonant frequency along the x–z plane at $y=0$ nm. The color contour shows the relative magnitude of the square of the y-component magnetic field. The vectors show the direction and magnitude of the electric field: (a) wire pattern ($l=0.5$ μm, $f_r=47.5$ THz), (b) cross pattern ($l=0.5$ μm, $f_r=50.8$ THz), and (c) square pattern ($l=1.7$ μm, $f_r=44.3$ THz).

inductance in the metal base plate are evaluated based on sheet resistance and inductance as discussed in the following. However, no distinction is given between the cross pattern and the wire pattern. The magnetic inductance or mutual inductance (L_m), which is originated from the magnetic energy stored in the dielectric spacer of distance d between the two parallel wires, has the form [29]

$$L_m = 0.5\mu_0 \frac{wd}{l} \tag{1}$$

where μ_0 is the permeability of vacuum. The (kinetic) impedance Z, which is originated from the kinetic energy of the electrons inside the metal, can be expressed as [29,30]

$$Z = R - i\omega L_k \tag{2}$$

where R and L_k are the resistance and kinetic inductance, respectively. The impedance can be evaluated by considering the complex conductivity of the material and an effective penetration depth, such that

$$Z = \frac{w}{(\sigma' + i\sigma'')A_{eff}} \tag{3}$$

where σ' and σ'' are the real and imaginary parts of complex conductivity, respectively, and A_{eff} is the effective cross section area of the induced electric current. For the top metallic pattern, $A_{eff} = \delta l$ and δ is an effective penetration depth of the electric field. Note that the penetration depth of the electric field is $\lambda/(2\pi\kappa)$, where κ is the extinction coefficient. Although a uniform distribution of
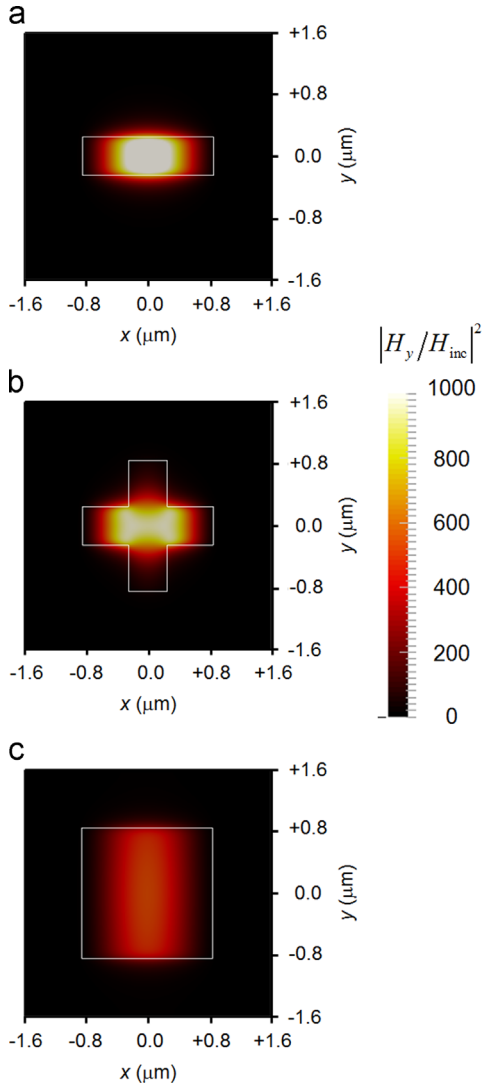
Fig. 4. Magnetic field profiles at the resonant frequency of the x–y cross section at the center of dielectric layer which is at $z=-120$ nm. The contour shows the relative magnitude of the square of the y-component magnetic field: (a) wire pattern ($l=0.5$ μm, $f_r=47.5$ THz), (b) cross pattern ($l=0.5$ μm, $f_r=50.8$ THz), and (c) square pattern ($l=1.7$ μm, $f_r=44.3$ THz).
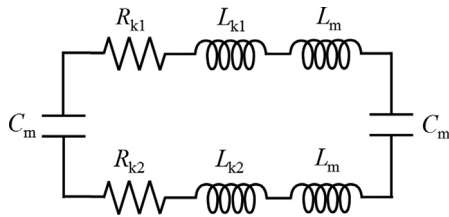
Fig. 5. The equivalent RLC circuit model between a metal strip and the base plate, separated by a dielectric spacer. Here, R_1 and L_{k1} are the resistance and kinetic inductance of the top strip, R_2 and L_{k2} are the resistance of the base plate, L_m is the mutual inductance, and C_m is the capacitance between the top strip and the bottom plate.

electric field is assumed in this equation, the non-uniformity of the field distribution needs to be considered. Therefore, an effective penetration depth is introduced by
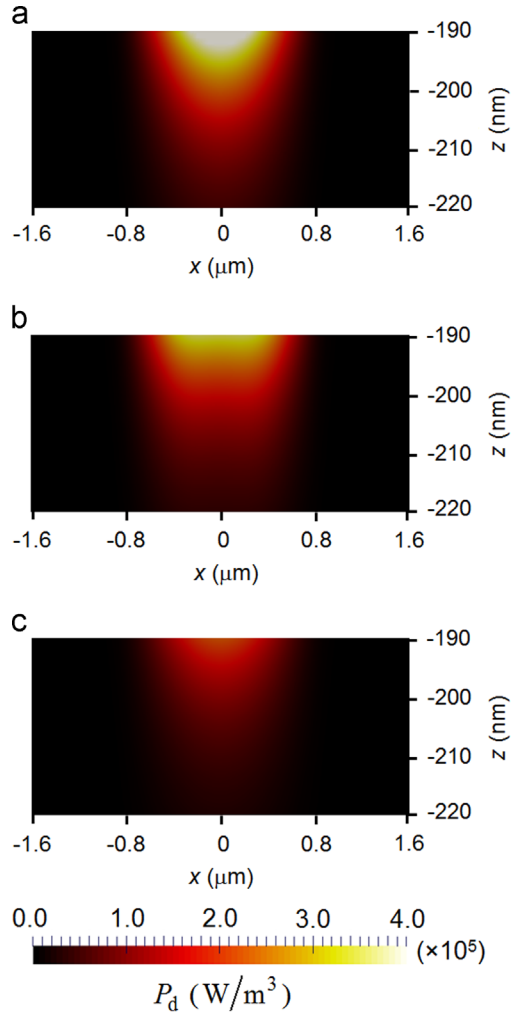
Fig. 6. Power dissipation density profiles at the resonant frequency of the x–z cross section at $y=0$ nm in the gold film: (a) wire pattern, (b) cross pattern, and (c) square pattern. The depth of x–z cross section is 30 nm below Al$_2$O$_3$/Au interface (the position of the interface is at $z=-190$ nm). The geometry and resonance conditions are the same as in Fig. 4.

using a factor c_1 so that

$$\delta = c_1 \lambda / (2\pi\kappa) \qquad (4)$$

The distribution of power absorbed per unit volume near the surface of metallic film is shown in Fig. 6 at the MP resonance frequency. The location at $z=-190$ nm corresponds to the Al$_2$O$_3$/Au interface. The power dissipation density can be calculated by [31]

$$P_d = \frac{1}{2}\varepsilon_0 \varepsilon'' \omega |\mathbf{E}|^2 \qquad (5)$$

The power dissipation density is related to the absorbed power per unit volume [W/m^3] or local Joule heating. In the calculations, the magnitude of electric field for the incident radiation is set to unity. The depth for the $1/e$ decay is about 20–25 nm at resonant frequencies as shown in Figs. 6a to c. Similar distributions and decay

lengths can be obtained for the top metallic structures whose thickness h is set to 100 nm. Note that the penetration depth calculated from $\lambda/(2\pi\kappa)$ is about 26 nm at the resonant frequency. In the present paper, $c_1 = 2/3$ is therefore adapted in estimating the penetration depth for both the top metal strip and the bottom metal plate. In the case of cross, it is modeled the same as a simple strip with a y-dimensional length of l since the main interest is to study the fundamental MP related to the width w. Using the relationship $\sigma' = \omega\varepsilon_0\varepsilon''$ and $\sigma'' = -\omega\varepsilon_0\varepsilon'$ [10], the resistance and kinetic inductance of top metallic pattern can be obtained as

$$R_1 = \frac{w}{\varepsilon_0\omega l\delta}\frac{\varepsilon''}{(\varepsilon'^2+\varepsilon''^2)} \tag{6}$$

$$L_{k1} = -\frac{w}{\varepsilon_0\omega^2 l\delta}\frac{\varepsilon'}{(\varepsilon'^2+\varepsilon''^2)} \tag{7}$$

where ε' and ε'' are respectively the real and imaginary parts of the complex dielectric function ε of the metal obtained from the optical constants tabulated in Palik [28]. The electrons are accumulated and oscillated within the top metallic pattern. However, the electrons are not confined the same way in the metallic film below the dielectric spacer. The current is allowed to flow in a wider pathway. Furthermore, the three-dimensionality of electromagnetic field affects the electric charge distribution near the surface of the metal film. Therefore, the concept of sheet resistance or impedance is employed by assuming that the induced electric current flow is along a square plate. Therefore the resistance and kinetic inductance in the metal film can be obtained by setting $l=w$ in Eqs. (6) and (7), resulting in

$$R_2 = \frac{1}{\varepsilon_0\omega\delta}\frac{\varepsilon''}{(\varepsilon'^2+\varepsilon''^2)} \tag{8}$$

$$L_{k2} = -\frac{1}{\varepsilon_0\omega^2\delta}\frac{\varepsilon'}{(\varepsilon'^2+\varepsilon''^2)} \tag{9}$$

In order to check the square sheet approximation, the power dissipation density is visualized at the x–y cross section in the metal film, as shown in Fig. 7, where the depth of cross section is 1 nm below Al_2O_3/Au interface ($z=-191$ nm). In Fig. 7a and b, the power dissipation profiles are broadly affected in the bottom metallic film compared to the top metallic patterns. For electric currents in the wire and cross patterns, they are obviously confined inside the top metallic strips as Fig. 4 shows. In the metal film, however, the electric currents may flow through a much wider breadth than the top pattern. Therefore, the square sheet approximation may better describe the current flow, although it is still a simplified approximation.

The dielectric spacer separating top metal pattern and the bottom metal film serves as a capacitor on each side, as shown in Figs. 3 and 4. The parallel-plate capacitance is expressed as

$$C_m = c_2\varepsilon_d\varepsilon_0\frac{wl}{d} \tag{10}$$

where $c_2 = 0.2$ is a numerical factor to consider the fringe effect or non-uniform charge distribution along the surfaces of capacitor. The capacitance between neighbor
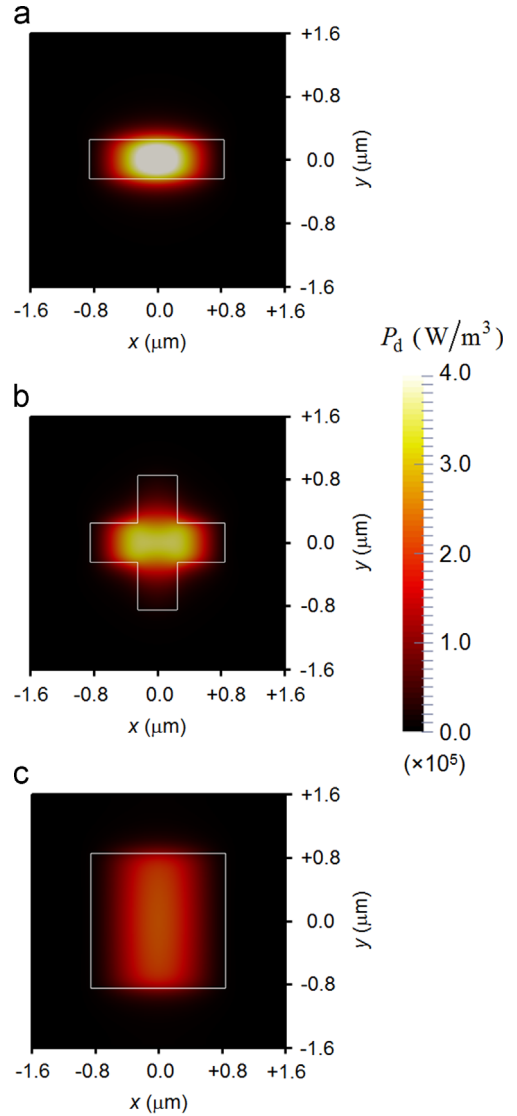
Fig. 7. Power dissipation density profiles at the resonant frequency of the x–y cross section at $z=-191$ nm in the gold film: (a) wire pattern, (b) cross pattern, and (c) square pattern. The depth of x–y cross section is 1 nm below Al_2O_3/Au interface. The geometry and resonance conditions are the same as in Fig. 4.

patterns is not included since it is negligible small compared with C_m [14]. The total impedance of RLC circuit model can be obtained as follows:

$$Z_{tot}(\omega) = R_1 + R_2 + \frac{2}{i\omega C_m} + i\omega(L_{k1}+L_{k2}) + 2i\omega L_m \tag{11}$$

Note that the penetration depth and dielectric function are wavelength-dependent. The resonance conditions for the fundamental MP mode can be obtained by zeroing the total impedance. The resonant frequency f_r, Q-factor Q, FWHM Δf of the circuit model can be expressed as [32]

$$f_r = \frac{1}{2\pi}\sqrt{\frac{2}{C_m(2L_m+L_{k1}+L_{k2})}} \tag{12}$$

$$Q = \frac{2}{R_1 + R_2} \sqrt{\frac{2L_m + L_{k1} + L_{k2}}{2C_m}} \qquad (13)$$

$$\Delta f = \frac{1}{2\pi} \left(\frac{R_1 + R_2}{2L_m + L_{k1} + L_{k2}} \right) \qquad (14)$$

This RLC circuit model is able to explain the geometric effects on the resonances in various metamaterials, which will be shown in the following section.

4. Results and discussion

The comparison between the results of FDTD and RLC model are shown in Fig. 8 for the metamaterial emitters or absorbers made of wire and cross pattern. Since the RLC circuit model treat both patterns as a strip (x-dimensional length w and y-dimensional length l) without considering the other strip in the cross pattern, the RLC prediction is the same for both patterns. As shown in Fig. 8a, the MP resonant frequencies predicted by the RLC model agree reasonably well with those from the FDTD simulation for values of l. The resonant frequency shifts to lower frequencies with increasing l. The previous studies using the LC circuit model could not capture this characteristic because the formulation used gave expressions that are independency of the length l [14–17,24]. The dependence of MP resonant frequencies on the length l can be understood by the fact that, a greater l will result in a larger values of $C_m L_{k2}$ in Eq. (12), thereby decreasing the MP resonant frequency. Note that the other terms $C_m L_m$ and $C_m L_{k1}$ are independent of l. It should be noted that according to FDTD, the resonant frequency of the cross pattern is always higher than that of the wire pattern for the same l. This may be explained by the additional strip in the cross pattern that is parallel to the y-axis that may produce an additional weak confinement of electromagnetic energy underneath the cross pattern. This weak confinement affects the main MP mode, resulting in an increased resonant frequency as compared with the wire pattern.

The predicted FWHMs also agree well with the FDTD simulation, especially the trend for varying the length l. As shown in Fig. 8b, the FWHMs become broader with larger l. The dependence of FWHM on the length l can be understood by the fact that, a larger l will give rise to a smaller value of the mutual inductance L_m and kinetic inductance L_{k1}, while L_{k2} is independent of l. Note that L_m is nearly twice that of L_{k1}; and $L_{k1} \geq L_{k2}$. According to the full-wave calculation, the bandwidth for the cross pattern is slightly broader than that of the wire pattern for the same l. This may be attributed to the aforementioned effect of the additional strip parallel to the y-axis. The coupling effect between the two strips may increase the FWHM of the cross-patterned metamaterial.

As shown in Fig. 8c, the predicted Q-factors from the RLC model also agree well with those from the FDTD simulation for varying length l. The Q-factors become smaller with increasing length l. It can be seen from Fig. 4 that the energy confinements of wire- and cross-patterned metamaterial are stronger than that of the square pattern metamaterial. This means that high Q-factors can be achieved with strong
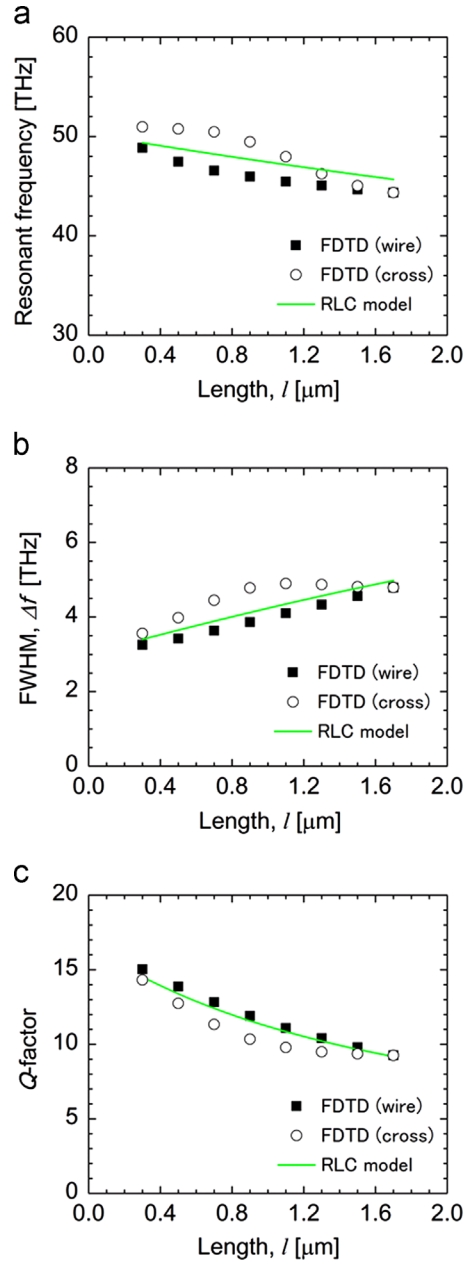
Fig. 8. Comparison with the FDTD results and the prediction by the RLC circuit model: (a) resonant frequency f_r, (b) FWHM Δf, and (c) Q-factor.

magnetic resonances, i.e., a smaller length l of the meta-materials. In other words, broader resonance peaks exist with the square pattern. While the discussion here is for a single resonance peak, the RLC circuit model could also be useful for understanding the resonant characteristics for the design of dual-, multi-, and broad-band metamaterial emitters and absorbers.

5. Conclusions

A simple RLC circuit model is built to explain the magnetic resonances in metamaterials with various top

metallic pattern length in the *y*-dimension. The main feature is to treat the resistance and kinetic inductance of the top patterned structure and the bottom film differently considering the field distributions. The predicted results are compared with that of FDTD simulation and good agreement in the predicted trends is obtained. As an extension of the LC circuit model, the modified RLC circuit model can reasonably predict the resonant characteristics such as resonant frequency, FWHM, and *Q*-factor of the MP resonant peaks. This study will benefit the understanding of magnetic resonances in metamaterial structures and facilitate the design of metamaterial absorbers and emitters.

Acknowledgments

References

[1] Fu CJ, Zhang ZM. Thermal radiative properties of metamaterials and other nanostructured materials: a review. Front Energy Power Eng China 2009;3:11–26.

[2] Zhang ZM, Wang LP. Measurements and modeling of the spectral and directional radiative properties of micro/nanostructured materials. Int J Thermophys 2013;34:2209–42.

[3] Watts CM, Liu XL, Padilla WJ. Metamaterial electromagnetic wave absorbers. Adv Mater 2012;24:OP98–120.

[4] Maruyama S, Kashiwa T, Yugami H, Esashi M. Thermal radiation from two-dimensionally confined modes in microcavities. Appl Phys Lett 2001;79:1393–5.

[5] Bermel P, Ghebrebrhan M, Chan W, Yeng YX, Araghchini M, Hamam R, et al. Design and global optimization of high-efficiency thermophotovoltaic systems. Opt Express 2010;18:A314–34.

[6] Sergeant NP, Agrawal M, Peumans P. High performance solar-selective absorbers using coated sub-wavelength gratings. Opt Express 2010;18:5525–40.

[7] Sakurai A, Tanikawa H, Yamada M. Computational design for a wide-angle cermet-based solar selective absorber for high temperature applications. J Quant Spectrosc Radiat Transf 2014;132:80–9.

[8] Liu N, Mesch M, Weiss T, Hentschel M, Giessen H. Infrared perfect absorber and its application as plasmonic sensor. Nano Lett 2010;10:2342–8.

[9] Pendry JB, Holden AJ, Robbins DJ, Stewart WJ. Magnetism from conductors and enhanced nonlinear phenomena. IEEE Trans Microw Theory Tech 1999;47:2075–84.

[10] Zhang ZM. Nano/microscale heat transfer. New York: McGraw-Hill; 2007.

[11] Landy NI, Sajuyigbe S, Mock JJ, Smith DR, Padilla WJ. Perfect metamaterial absorber. Phys Rev Lett 2008;100:207402.

[12] Liu XL, Tyler T, Starr T, Starr AF, Jokerst NM, Padilla WJ. Taming the blackbody with infrared metamaterials as selective thermal emitters. Phys Rev Lett 2011;107:045901.

[13] Aydin K, Ferry VE, Briggs RM, Atwater HA. Broadband polarization-independent resonant light absorption using ultrathin plasmonic super absorbers. Nat Commun 2011;2:517.

[14] Wang LP, Zhang ZM. Wavelength-selective and diffuse emitter enhanced by magnetic polaritons for thermophotovoltaics. Appl Phys Lett 2012;100:063902.

[15] Wang LP, Zhang ZM. Measurement of coherent thermal emission due to magnetic polaritons in subwavelength microstructures. J Heat Transf 2013;135:091505.

[16] Zhao B, Wang LP, Shuai Y, Zhang ZM. Thermophotovoltaic emitters based on a two-dimensional grating/thin-film nanostructure. Int J Heat Mass Transf 2013;67:637–45.

[17] Wang H, Wang LP. Perfect selective metamaterial solar absorbers. Opt Express 2013;21:A1078–93.

[18] Bouchon P, Koechlin C, Pardo F, Haidar R, Pelouard JL. Wideband omnidirectional infrared absorber with a patchwork of plasmonic nanoantennas. Opt Lett 2012;37:1038–40.

[19] Hendrickson J, Guo JP, Zhang BY, Buchwald W, Soref R. Wideband perfect light absorber at midwave infrared using multiplexed metal structures. Opt Lett 2012;37:371–3.

[20] Engheta N. Circuits with light at nanoscales: optical nanocircuits inspired by metamaterials. Science 2007;317:1698–702.

[21] Chen H-T. Interference theory of metamaterial perfect absorbers. Opt Express 2012;20:7165–72.

[22] Zhu L, Sandhu S, Otey C, Fan SH, Sinclair MB, Luk TS. Temporal coupled mode theory for thermal emission from a single thermal emitter supporting either a single mode or an orthogonal set of modes. Appl Phys Lett 2013;102:103104.

[23] Zhou J, Economon EN, Koschny T, Soukoulis CM. Unifying approach to left-handed material design. Opt Lett 2006;31:3620–2.

[24] Sakurai A, Zhao B, Zhang ZM. Prediction of the resonance condition of metamaterial emitters and absorbers using LC circuit model. In: Proceedings of 15th international heat transfer conference, 2014, IHTC15-9012, 1-10.

[25] Fu L, Schweizer H, Guo H, Liu N, Giessen H. Synthesis of transmission line models for metamaterial slabs at optical frequencies. Phys Rev B 2008;78:115110.

[26] Zhou J, Koschny T, Soukoulis CM. An efficient way to reduce losses of left-handed metamaterials. Opt Express 2008;16:11147–52.

[27] Penciu RS, Kafesaki M, Koschny T, Economou EN, Soukoulis CM. Magnetic response of nanoscale left-handed metamaterials. Phys Rev B 2010;81:235111.

[28] Palik ED. Handbook of optical constants of solids. San Diego: Academic Press; 1998.

[29] Wang LP, Zhang ZM. Phonon-mediated magnetic polaritons in the infrared region. Opt Express 2011;19:A126–35.

[30] Zhao B, Zhang ZM. Study of magnetic polaritons in deep gratings for thermal emission control. J Quant Spectrosc Radiat Transf 2014;135:81–9.

[31] Hao J, Zhou L, Qiu M. Nearly total absorption of light and heat generation by plasmonic metamaterials. Phys Rev B 2011;83:165107.

[32] Solymar L, Shamonina E. Waves in metamaterials. Oxford: Oxford University Press; 2009.